Finding transition states for crystalline solid–solid phase transformations

Kyle J. Caspersen and Emily A. Carter*

Department of Mechanical and Aerospace Engineering and Program in Applied and Computational Mathematics, Princeton University, Princeton, NJ 08544-5263

Edited by Bruce J. Berne, Columbia University, New York, NY, and approved March 14, 2005 (received for review November 1, 2004)

We present a method to identify transition states and minimum energy paths for martensitic solid–solid phase transformations, thereby allowing quantification of the activation energies of such transformations. Our approach is a generalization of a previous method for identifying transition states for chemical reactions, namely the climbing image-nudged elastic band algorithm, where here the global deformation of the crystalline lattice (volume and shape fluctuations) becomes the reaction coordinate instead of atomic motion. We also introduce an analogue to the Born–Oppenheimer approximation that allows a decoupling of nuclear motion and lattice deformation, where the nuclear positions along the path are determined variationally according to current deformation state. We then apply this technique to characterize the energetics of elemental lithium phase transformations as a function of applied pressure, where we see a validation of the Born–Oppenheimer-like approximation, small energy barriers (expected for martensitic transformations), and a pronounced pressure dependence of various properties characterizing the phase transitions.

martensitic | phase transitions | transition state search

Activated processes have long been a subject of study, with the most obvious example consisting of the field of gaseous and liquid phase chemical reaction kinetics. In gas phase kinetics, the collection of atoms or ions follows a trajectory from reactant to product. If the configuration of atoms at some point along the trajectory is more energetic than the reactant or the product, the process is said to be activated. The specific trajectory that provides the smallest energy increase is termed the minimum energy path (MEP), where the point along the path that yields the highest energy is termed the transition state (TS) and the energy difference between the reactants and the TS is called the activation energy (E_{act}). The TS is also characterized by being a saddle point in potential energy space, where the gradient is zero and only one direction of negative curvature is present. Then, according to transition state theory (1), the rate of the reaction (z) may be described by a simple Arrhenius form $z = \nu\exp[-E_{act}/k_BT]$, where T is the temperature, k_B is the Boltzmann constant, and ν is a term representing the attempt frequency.

The MEP in principle is indexed by the coordinates of the entire nuclear and electronic wave-function. However, very often the system is in its electronic ground state along the MEP, and the nuclear motion is slow enough for the Born–Oppenheimer approximation (2) to be valid. Therefore, in practice the MEP is often indexed only by the $3N$-6 degrees of freedom describing the nuclear positions.

Many techniques have been developed for finding fluid phase TSs and their corresponding E_{act}s. They include, but are not limited to, the drag (or reaction coordinate) method (a description can be found in ref. 3), the ridge method (4, 5), various band methods (3, 6–8), and the dimer method (9). These methods were developed for finite, nonperiodic systems with a static reference frame, such as isolated molecules reacting in a dilute gas.

In the present work, we consider a different class of activated processes, namely activated solid–solid phase transformations that occur via a diffusionless cooperative movement of all atoms in a transformation region. Such phase transformations are referred to as martensitic and are commonly experienced by many important materials, including steel, various shape memory alloys, and oxide ceramics such as zirconia. Whereas atomic-scale nucleation-driven phase transformations involve a localized, nonperiodic event, martensitic phase transitions effectively require consideration of a three-dimensional, periodically infinite crystal to correctly describe the collective atomic motion. By contrast to the fluid phase case, here the frame of reference changes. In particular, the cell lattice vectors of the repeating unit of the crystal deform during the transformation.

This observation suggests that the MEP should be not only a function of the nuclear positions but also of the unit cell lattice vectors. Unfortunately, most previous algorithms for finding transition states were not designed to describe a periodic system in which the cell vectors may vary. One algorithm that does do this during a transition state search was proposed recently by Trinkle *et al.* (10, 11). They used the standard nudged elastic band (NEB) technique (3) for nonperiodic systems, with the modification that the cell vectors along the path were minimized with respect to the stress via standard Parrinello–Rahman molecular dynamics techniques (12–14). This method assumes that nuclear motion controls the phase transformation, and that the deformation of the cell vectors follows the nuclear motion as an implicit function of the nuclear coordinates. However, in the case of a martensitic phase transformation, it is likely the other way around: A microscopic deformation will be imposed on the cell vectors, which in turn will dictate the constraints on the nuclear coordinates. Thus, the nuclear coordinates should evolve along a pathway set by the microscopic deformation, which is the reverse of the approach described in refs. 10 and 11. Also, it is not obvious that the stress should be minimized along the nuclear coordinate path, as done in the method described in refs. 10 and 11. Therefore, although the approach used in the work detailed in refs. 10 and 11 will predict a mechanism for a phase transformation, it may not be physically realistic. For example, it may not produce smoothly varying cell vectors along the predicted transformation path.

By contrast, we present a method for finding transition states for martensitic phase transformations where the phase transformation mechanism is explicitly dependent on the deformation gradient; the latter quantity, in turn, dictates the physical constraints on the nuclear positions. In what follows, we describe the method and then apply it to phase transitions in elemental Li as a function of pressure. We begin with a review of the nonperiodic transition state search algorithm known as the climbing image-nudged elastic band (CINEB) approach (8), on which our method is based.

Background: The Climbing Image-Nudged Elastic Band

The basic premise for finding TS is the same for almost all techniques that have been developed previously (with the dimer

This paper was submitted directly (Track II) to the PNAS office.

Abbreviations: CINEB, climbing image-nudged elastic band; EB, elastic band; MEP, minimum energy path; NEB, nudged elastic band; OF DFT, orbital-free density functional theory; SSNEB, solid-state nudged elastic band.

*To whom correspondence should be addressed. E-mail: eac@princeton.edu.

www.pnas.org/cgi/doi/10.1073/pnas.0408127102

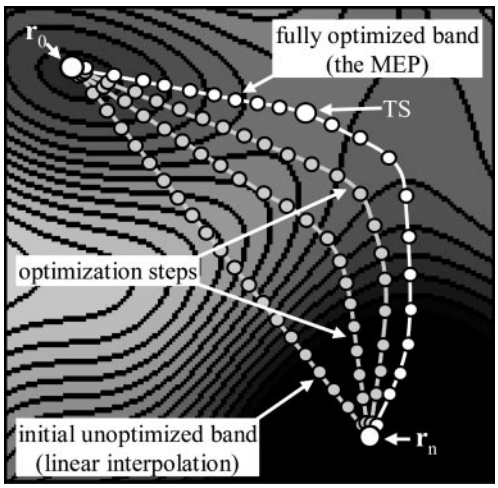

Fig. 1. Schematic of an ideal EB method. This shows a linear interpolation as the initial unoptimized band, two optimization steps, and the fully optimized band that represents the MEP, which contains the TS.

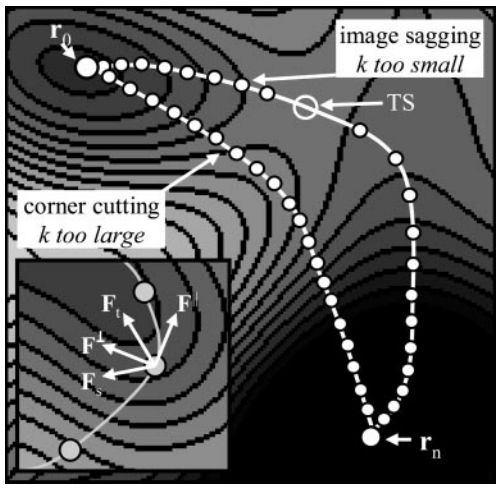

Fig. 2. Schematic of the drawbacks of the pure EB method, namely ''image sagging'' and ''corner cutting.'' (*Inset*) Particular force components.

method as a notable exception). First, the structure of the transition state is approximated, and then a constrained minimization is performed, where the imposed constraints allow the system to relax to the TS rather than to a local energy minimum. This constrained minimization premise should also apply to crystalline transformations, allowing us to simply generalize earlier constrained optimization algorithms, e.g., the CINEB scheme.

In the CINEB method, the initial and final (reactant and product) states must be identified in advance. In particular, we must enumerate the configurations of the atoms, $\mathbf{r}_0$ and $\mathbf{r}_n$, for the initial and final states, respectively. After the initial and final states are identified, a series of ''images'' $\mathbf{r}_0 \ldots \mathbf{r}_n$ are formed. These images are slight deviations of $\mathbf{r}_0$ and $\mathbf{r}_n$, most commonly constructed by a linear interpolation of the form $\mathbf{r}_m = \mathbf{r}_0 + m/n\,(\mathbf{r}_n - \mathbf{r}_0)$. There is a natural force that drives each image toward either $\mathbf{r}_0$ and $\mathbf{r}_n$, since $\mathbf{r}_0$ and $\mathbf{r}_n$ are stable minima, whereas points in between are not. This natural driving force is termed the ''true force'' ($\mathbf{F}_t$), which is the negative of the potential energy gradient with respect to the nuclear positions, $\mathbf{F}_t = -\partial E/\partial \mathbf{r}$. As mentioned above, a constraint must be imposed to find the transition state such that the relaxation of these images results in movement not toward $\mathbf{r}_0$ or $\mathbf{r}_n$ but, rather, toward the transition state structure. This constraint in CINEB is termed the ''spring force,'' given by the negative of the gradient of some constructed ''spring energy'': $E_s = \Sigma_m k_s(\mathbf{r}_{m+1} - \mathbf{r}_m)^2$, where k_s is the ''spring constant'' with a corresponding spring force $\mathbf{F}_s = -\partial E_s/\partial \mathbf{r}$. These two equations complete the description of a predecessor to CINEB termed the elastic band (EB) method (6, 7), where the total force is given by $\mathbf{F} = \mathbf{F}_t + \mathbf{F}_s$. Fig. 1 is a schematic description of this method, where it is easily seen that a simple physical analogue to this method would be a series of weighted beads connected by springs.

The EB method generally does not find the exact transition state because of two significant problems, which in fact are properties of an actual set of beads and springs (see Fig. 2). The first problem is termed ''image sagging,'' which occurs when the spring constant, k_s, is too small. In this case, the images will sag away from the TS, producing low resolution around the TS and an artificially small E_{act}. The second problem is termed ''corner cutting,'' which occurs when k_s is too large. Here, the band cannot relax to the TS, producing an artificially large E_{act}. In fact, it is not possible to choose a k_s that alleviates both problems. The solution comes from the realization that the two problems are due to specific components of the force (Fig. 2 *Inset*), which can be identified by defining a smooth multidimensional curve passing through the images. This allows $\mathbf{F}_t$ and $\mathbf{F}_s$ to be decomposed into force components that run parallel ($\mathbf{F}^{\parallel}$) and perpendicular ($\mathbf{F}^{\perp}$) to the curve's tangent, i.e., $\mathbf{F} = \mathbf{F}^{\parallel} + \mathbf{F}^{\perp}$. The decomposition brings the intuitive conclusion that image sagging is a consequence of the parallel component of $\mathbf{F}_t$ and that corner cutting is due to the perpendicular component of $\mathbf{F}_s$. The solution is provided by simply projecting out the two problematic components of the force, leaving the total force used by the search algorithm to be $\mathbf{F} = \mathbf{F}_t^{\perp} + \mathbf{F}_s^{\parallel}$. This projected force results in evenly spaced images with no image sagging and allows the band to ''slide down'' to the TS with no corner cutting. Employing these force projections, referred to as nudging, is an extension of the EB method, termed the nudged elastic band (NEB) technique (3).

The NEB method does have one significant drawback. Unless precisely the correct number of images is chosen initially such that the image spacing along the MEP yields one image in the relaxed band resting directly on top of the TS, the E_{act} will be artificially low. This is problem is solved by simply zeroing the spring force on, and applying the negative of the parallel component of the true force to, the highest-energy image. This means that the force on the highest-energy image, and *only* the highest-energy image, will be $\mathbf{F} = \mathbf{F}_t^{\perp} - \mathbf{F}_t^{\parallel}$. This force results in the highest-energy image, or climbing image, being driven to the TS. This entire procedure is termed the climbing image-nudged elastic band (CINEB) technique (8).

The Solid-State Nudged Elastic Band

To generalize the CINEB technique to find TS for solid–solid phase transformations, we need to recast the true and spring forces appropriately, by accounting for the additional degrees of freedom due to the global crystalline deformation during the phase transformation. As mentioned above, this implies that we must account for $3N$ parameters. To avoid this level of complexity, we make an approximation that greatly reduces this number of degrees of freedom.

The approximation we impose is in the spirit of the Born–Oppenheimer approximation, which exploits the fact that electronic motion generally is much faster than nuclear motion, thereby allowing for a separation of time scales between the two. This approximation also implies a corollary in which the nuclear forces for any configuration are dependent on only a steady state (usually the equilibrium ground state) electronic configuration. By analogy, we assert that the nuclear (and thus the electronic) motion may be decoupled from the global crystal deformation ($\mathbf{U}$). It follows that mechanical properties of the crystal, specifically the stress tensor, may be characterized by a zero force state

on the nuclei. The specific zero force state we consider is the ground electronic and nuclear state for a particular **U**. Since there is likely only one ground state nuclear and electronic configuration, the system then will be described completely by the global deformation gradient. This approximation reduces the degrees of freedom from $3N$ to 6,[†] provided no external field exists. We term this approximation the rapid nuclear motion (RNM) approximation, which results in the atomic positions being implicitly dependent on the deformation gradient.

This RNM approximation is valid for cases in which only the total energy is relevant, where there is likely only one nuclear configuration at zero Kelvin. However, for finite temperature (i.e., molecular dynamics) simulations, there is an ensemble of nuclear configurations and associated velocities that are consistent with a particular temperature. Each nuclear configuration results in a different stress tensor; therefore, it is not possible to separate the nuclear and lattice degrees of freedom, i.e., the RNM approximation is not valid for finite temperatures. Techniques for finite temperature simulations with a "breathing" reference frame have been mentioned above (12–14).

To use the CINEB scheme within the RNM approximation, analogues of the true and spring forces must be identified. The true force for the nonperiodic system is the force due to the nuclear position potential, $\mathbf{F}_t = -\partial E/\partial \mathbf{r}$. The analogous "force" on the crystal unit cell due to deformations of the cell vectors, **h**, is given by the stress tensor $\boldsymbol{\sigma}_t = -\partial E/\partial \mathbf{h}$. We call $\boldsymbol{\sigma}_t$ the "true stress," defined by $\boldsymbol{\sigma}_t = -\Omega(\boldsymbol{\sigma}_{\text{cauchy}} + \mathrm{P}\cdot\mathbf{I})(\mathbf{h}^{-1})^T$, where Ω is the cell volume, $\boldsymbol{\sigma}_{\text{cauchy}}$ is the Cauchy stress tensor [defined as $\boldsymbol{\sigma}_{\text{cauchy}} = \Omega^{-1}(\partial E/\partial \mathbf{h})\mathbf{h}^T$], and P is the external pressure. Defining $\boldsymbol{\sigma}_t$ in such a manner lets us write the cell reshaping equation as $\mathbf{h}' = \mathbf{h} + \boldsymbol{\sigma}_t\,\Delta t$, where Δt is an arbitrary time step.

The CINEB scheme also requires an analogue to the spring force. We accomplish this by defining a total spring energy for the band to be $E_{\text{spring}} = k_s \sum_{i=1}^{N-1} \boldsymbol{\varepsilon}_i : \boldsymbol{\varepsilon}_i$. Here, : is the double dot product,[‡] and k_s is a spring constant. If $\mathbf{h}_i$ and $\mathbf{h}_{i+1}$ are neighboring images and **I** is the identity matrix, then the strain $\boldsymbol{\varepsilon}_i$ is defined by $\mathbf{h}_{i+1} = (\mathbf{I} + \boldsymbol{\varepsilon}_i)\mathbf{h}_i$. Then, the analog of the spring force is the spring stress $\boldsymbol{\sigma}_s = -\partial E_{\text{spring}}/\partial \mathbf{h}$. Accounting for $\boldsymbol{\sigma}_s$ results in an analogue of the EB with a reshaping equation of the form $\mathbf{h}' = \mathbf{h} + (\boldsymbol{\sigma}_t + \boldsymbol{\sigma}_s)\Delta t$.

To complete the definition of the generalized CINEB scheme for phase transformations, an analogy for the tangent to the MEP must be defined that is consistent with the definitions of $\boldsymbol{\sigma}_s$ and $\boldsymbol{\sigma}_t$. We form the tangent by first fitting nine interpolating cubic spline functions, one for each component of **h**. The independent variable for the spline fit for any image was defined to be the distance along the band in strain space ($\Delta\varepsilon$), defined as $\Delta\varepsilon_i = (\boldsymbol{\varepsilon}_i : \boldsymbol{\varepsilon}_i)^{1/2} + \Delta\varepsilon_{i-1}$, where $\Delta\varepsilon_0 = 0$. This allows us to represent the spline functions as $\xi^{\alpha\beta}(\Delta\varepsilon)$, where $\alpha\beta$ represent one of the nine components of **h**. The tangent tensor for image i and components $\alpha\beta$ ($\tau_i^{\alpha\beta}$) is then represented by $\boldsymbol{\tau}_i^{\alpha\beta} = d\xi^{\alpha\beta}/d\Delta\varepsilon$ evaluated at $\Delta\varepsilon_i$, where $\boldsymbol{\tau}_i$ is a 3×3 matrix. This then allows us to perform the force projections (nudging) to keep constant image spacing, where the projections of the $\boldsymbol{\sigma}_t$ and $\boldsymbol{\sigma}_s$ parallel to the tangent are defined as $\boldsymbol{\sigma}^{\parallel} = (\boldsymbol{\sigma} : \boldsymbol{\tau}/\boldsymbol{\tau} : \boldsymbol{\tau})\boldsymbol{\tau}$. It follows that the projections perpendicular to the tangent are simply $\boldsymbol{\sigma}^{\perp} = \boldsymbol{\sigma} - \boldsymbol{\sigma}^{\parallel}$. We can now define the NEB reshaping equation as $\mathbf{h}' = \mathbf{h} + (\boldsymbol{\sigma}_t^{\perp} + \boldsymbol{\sigma}_s^{\parallel})\Delta t$. To complete the generalization of the CINEB, a climbing image must be introduced, which is accomplished by changing the reshaping equation of the highest energy image to be $\mathbf{h}' = \mathbf{h} + (\boldsymbol{\sigma}_t^{\perp} - \boldsymbol{\sigma}_t^{\parallel})\Delta t$, in direct analogy with the CINEB scheme for the nonperiodic case.

[†]The deformation gradient does have 9 components; however, the invariance of the energy to rigid body rotations allows 3 degrees of freedom to be removed.

[‡]If G and H are two matrices with identical dimension a and b, then the double dot product is defined as $\sum_{i=1}^{a}\sum_{j=1}^{b} G_{ij}H_{ij}$.

Validation

To validate this new method, which we term the solid-state–nudged elastic band (SSNEB) technique, we investigate solid–solid phase transformations in lithium. The pressure–temperature phase diagram for Li (15) shows that Li exists in the complex close-packing arrangement hex(9) near zero P and T. A pressure-driven phase transformation exists at ≈3 GPa, where the hex(9) phase transforms into an *fcc* phase. The *bcc* phase of Li is formed through a temperature-driven phase transformation at ≈90 K. The *bcc* to close-packed transformations show martensitic behavior (16) and thus should be good test cases for the SSNEB technique.

Transformation Paths. In traditional energy minimizations involving routine geometry optimizations, the choice of initial conditions is important because such searches are only guaranteed to find a local, not global, minimum. It is therefore not surprising that constrained minimizations involved in TS searches also have a strong dependence on the initial conditions, leading to the nearest TS on the potential energy hypersurface. Typically for energy minimizations, an educated guess of the full optimized geometry is used as a starting point. However, the initial conditions for all of the band methods are more complex, consisting of an approximation of the entire MEP. Analogously, we must approximate the full phase transformation path in our SSNEB approach. Since we are applying the RNM approximation discussed above, the transformation path is a function of only the cell vectors, which means the overall transformation is described by a deformation gradient, **U**. We then use **U** to form the initial conditions, where we choose initial images along the band to be a linear segmentation of **U** from the initial to the final state.

For the *bcc* to *fcc* transformation, the initial state is the two-atom *bcc* cubic unit cell $\mathbf{h}_{bcc} = a_0\mathbf{I}$, where **I** is the identity and a_0 is the *bcc* lattice constant. The two atoms, labeled $\mathbf{r}_{bcc}^{\mathrm{I}}$ and $\mathbf{r}_{bcc}^{\mathrm{II}}$, are positioned in fractional coordinates at (0 0 0) and (½ ½ ½), respectively. This choice of lattice vectors allows the transformation path to be described simply as a uniaxial expansion along one of the lattice vectors. The deformation gradient for this transformation $\mathbf{U}_{bcc\to fcc}$ is simply

$$\mathbf{U}_{bcc\to fcc} = \beta\begin{pmatrix} 1 & 0 & 0 \\ 0 & 1 & 0 \\ 0 & 0 & \sqrt{2} \end{pmatrix}, \qquad [1]$$

with the density of the resulting *fcc* phase controlled by the parameter β, which has the form $\beta = 2^{1/6} V_{fcc}^{1/3} V_{bcc}^{1/3}$, where V_X is the volume per atom of phase X. To complete the description of the resulting *fcc* phase, we note that the fractional coordinates of the atoms are unchanged during the transformation, i.e., $\mathbf{r}_{fcc}^{\mathrm{I}} = (0\ 0\ 0)$ and $\mathbf{r}_{fcc}^{\mathrm{II}} = (\tfrac{1}{2}\ \tfrac{1}{2}\ \tfrac{1}{2})$.

Unlike the *bcc* to *fcc* transformation, the *bcc* to *hcp* transformation cannot be described with the two-atom *bcc* cubic unit cell. Instead, the *bcc* to *hcp* transformation is most easily represented by the two-atom *bcc* hexagonal unit cell, where the *bcc* lattice vectors will be given by

$$\mathbf{h}_{bcc} = \frac{a_0}{2}\begin{pmatrix} 2 & 1 & 0 \\ 0 & \sqrt{2} & 0 \\ 0 & 0 & 2\sqrt{2} \end{pmatrix}. \qquad [2]$$

The fractional coordinates of the ions are then $\mathbf{r}_{bcc}^{\mathrm{I}} = (0\ 0\ 0)$ and $\mathbf{r}_{bcc}^{\mathrm{II}} = (\tfrac{1}{2}\ 0\ \tfrac{1}{2})$.

The *bcc* to *hcp* transformation mechanism we employ here is the well known Burgers path (17). This mechanism is most succinctly described as a two-step process.[§] A shear deformation, $\mathbf{U}_{bcc\to hcp}$, is

[§]In actuality, the two steps in this mechanism occur relatively simultaneously. We break them apart simply for ease of discussion.

first applied to $\mathbf{h}_{bcc}$ to form $\mathbf{h}_{hcp}$, with the latter being a staggered hexagonal lattice. With respect to the cubic unit cell, $\mathbf{U}_{bcc\rightarrow hcp}$ consists of a compression along a ⟨100⟩ direction and an elongation along an orthogonal ⟨110⟩ direction. The hexagonal *bcc* cell given above yields a simple representation of $\mathbf{U}_{bcc\rightarrow hcp}$, where

$$\mathbf{U}_{bcc\rightarrow hcp} = \frac{\gamma}{4}\begin{pmatrix} 2\sqrt{3} & 0 & 0 \\ 0 & 3\sqrt{2} & 0 \\ 0 & 0 & 4\alpha \end{pmatrix}. \qquad [3]$$

Like the β for $\mathbf{U}_{bcc\rightarrow fcc}$, γ controls the density of the *hcp* phase and is of the form $\gamma = [(4\sqrt{6}V_{hcp})/(9\alpha V_{bcc})]^{1/3}$, where $\alpha = (3/8)^{1/2}(c/a)$ and c/a is the ratio of the two distinct lattice vectors. The application of $\mathbf{U}_{bcc\rightarrow hcp}$ to $\mathbf{h}_{bcc}$ produces the *hcp* lattice vectors as

$$\mathbf{h}_{hcp} = \frac{a_0\gamma}{4}\begin{pmatrix} 2\sqrt{3} & \sqrt{3} & 0 \\ 0 & 3 & 0 \\ 0 & 0 & \alpha 4\sqrt{2} \end{pmatrix}. \qquad [4]$$

As mentioned above, $\mathbf{U}_{bcc\rightarrow hcp}$ forms a staggered hexagonal lattice. To form the equilibrium *hcp* lattice, alternating hexagonal layers must be shuffled by a vector $\mathbf{u} = (0\ \frac{1}{4}\ 0)$, in the *bcc* reference frame. In our representation, this accomplished by applying $\mathbf{u}$ to one of the two atoms in the cell, namely $\mathbf{r}^{\mathrm{II}}$, in the *bcc* reference frame. The fractional coordinates of the two atoms are thus $\mathbf{r}^{\mathrm{I}}_{hcp} = (0\ 0\ 0)$ and $\mathbf{r}^{\mathrm{II}}_{hcp} = (\frac{1}{3}\ \frac{1}{3}\ \frac{1}{2})$. Eqs. **1–4** complete the definitions of the phase transformation paths we consider in these first applications of the SSNEB method.

Calculational Details. Care must be taken when choosing a minimization algorithm; this is not only true for the SSNEB but also for any NEB method. The act of nudging (i.e., using the force projections) means that the optimized band is *not* at an energy minimum of the potential energy surface dictated by the true and spring stresses but, rather, at a stable point of a related but different hypersurface. Therefore, algorithms that are tailored for fast energy minimizations (e.g., conjugate gradient, quasi-Newton, etc.) have little meaning. The best optimization algorithms for our purposes are those where the update step only depends on the "force," or the stress in our case. Here, we use a steepest descent algorithm that requires a line optimization. Let ω be a vector containing all nine components of $\boldsymbol{\sigma}_{\mathrm{t}}^{\perp} + \boldsymbol{\sigma}_{\mathrm{s}}^{\parallel}$ for all of the images on the band (for the climbing image, $\boldsymbol{\sigma}_{\mathrm{t}}^{\perp} - \boldsymbol{\sigma}_{\mathrm{t}}^{\parallel}$ is used instead); therefore, if there are N images, ω will be $9N$-dimensional. If ω_0 is the initial vector and ω_n is the vector after n line minimizations, then ω_n^{L} is the projected stress along the line search direction for step n, where $\omega_n^{\mathrm{L}} = \omega_0(\omega_n\cdot\omega_0/\omega_0\cdot\omega_0)$. Each line search is terminated when $|\omega_n^{\mathrm{L}}| \approx 0$, in other words when ω_0 and ω_n are said to be "orthogonal." (Note that this termination condition is valid for non-nudged systems as well. However, unlike non-nudged systems, the termination point is not necessarily an energy minimum along the search direction.) Progressive line searches are performed until $|\omega_n| \approx 0$, at which point the band is optimized.

The key quantity in updating and ultimately optimizing the band is the calculation of the stress tensor. As mentioned above, we use the RNM approximation, which allows the stress tensor to be completely defined as a function of the lattice vectors. As a result, the nuclear coordinates must be optimized before the stress tensor can be extracted. We employ the conjugate gradient method to perform this optimization of the nuclear positions.

Since we apply the Born–Oppenheimer approximation for the electrons and nuclei, we require the electronic degrees of freedom to be optimized as well, to calculate the nuclear forces (needed to optimize the nuclear positions) and the resulting stress tensor. In this work, we use a first-principles quantum mechanics method known as orbital-free density functional theory (OF DFT) to solve directly for the electronic ground state (18). OF DFT is a very fast linear scaling DFT method that utilizes an approximate form for the kinetic energy of the electrons. The particular form of the so-called kinetic energy density functional (KEDF) used here provides meV per atom accuracy for main group, nearly free-electron-like metals. In particular, we use the Wang–Govind–Carter KEDF with a density-dependent response kernel (19). The other approximation inherent in OF DFT is the need to use a local (non-angular-momentum-dependent) "pseudopotential" for describing the interaction of the valence electrons with the nuclei and core electrons. Here, we use a local pseudopotential for Li that was validated in earlier OF DFT simulations (20, 21). We used the local density approximation to describe electron exchange and correlation (22, 23); it has been shown by several authors that for metals, the local density approximation yields properties as reliable as gradient-corrected exchange-correlation functionals (24, 25). Because the OF DFT method solves directly for the electron density instead of for a wave-function, there is no k-point sampling in these calculations, resulting in substantial time savings for metallic systems. The calculations were fully converged with respect to kinetic energy cutoff of the plane wave expansion of the density ($E_{\mathrm{cut}} = 90$ Ryd), yielding total energies converged to within 0.0005 eV per atom. The convergence criterion for band optimization was that the magnitude of the total stress tensor ($|\boldsymbol{\sigma}_{\mathrm{tot}}|$), defined as $|\boldsymbol{\sigma}_{\mathrm{tot}}| = (\boldsymbol{\sigma}_{\mathrm{tot}}:\boldsymbol{\sigma}_{\mathrm{tot}})^{1/2}$, for any image, must be <0.001 eV/Å^3, where $\boldsymbol{\sigma}_{\mathrm{tot}}$ is the total nudged force on the image cell vectors.

In theory, the climbing image for the SSNEB method can be used from the first iteration onward. However, in practice it is more efficient to relax the band first by using the NEB method up to some tolerance and then "turn on" the climbing image to complete the relaxation of the full band. This is especially important for systems in which the fractional coordinates of the nuclei change, since the nuclear position optimization required under the RNM approximation can be expensive. In particular, the nuclear positions tend to change most near the transition state. Therefore, it is most efficient to only turn on the climbing image near the end, to minimize the cost of optimization of the nuclear degrees of freedom.

Results. Predicted properties along the *bcc* to *fcc* transformation path under varying ambient pressure conditions are shown in Fig. 3. The independent variable in this figure (Δ) is called the reaction coordinate and generally has arbitrary units; in our case, Δ represents the distance along the band in strain space. $\Delta = 0$ represents the completely relaxed *bcc* phase, and the maximum value of Δ represents the completely relaxed *fcc* phase. It should be noted that the fractional coordinates of the atoms do not change at any point along the MEP for any pressure, implying no loss of symmetry.

Fig. 3*a* displays the energy per atom along the MEP with respect to the relaxed *bcc* phase at various specific pressures. Consistent with the experimental phase diagram, the *fcc* phase is found to be lower in energy than the *bcc* phase at 0–10 GPa. We predict that the phase ordering will be reversed at very high pressures; the phase reversal may be real, or it could indicate a breakdown of OF DFT, or more likely a breakdown of the pseudopotential approximation at high pressures. (Note that this does not imply any problem with the method but, rather, with standard solid state electronic structure approximations, which are not the subject of this work.) The energy varies smoothly along the MEP for all pressures. We observe that as the pressure increases, the E_{act} for the *bcc* to *fcc* transformation increases and the TS moves closer to the *fcc* phase. These two results are quantified in Fig. 4, where Fig. 4*a* shows that the *bcc* to *fcc* E_{act} increases by a factor of 4, from 0.0005 eV per atom at zero pressure to 0.002 eV per atom at 50 GPa. The *fcc* to *bcc* E_{act} has a slight downward trend but remains relatively flat, only varying $\approx$0.0005 eV per atom over this pressure range. These very small E_{act} are to be expected for martensitic phase transformations; given the large number of atoms involved in the collective motion of the

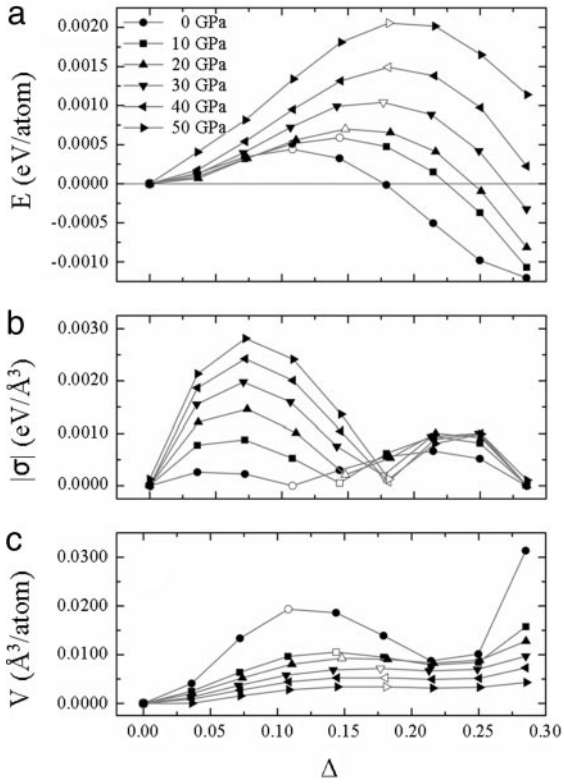

Fig. 3. Predicted properties of the *bcc* to *fcc* transformation for varying ambient pressure conditions. The energy per atom (*E*), the magnitude of true stress (|σ|), and the volume per atom (*V*) along the MEP are shown in *a*–*c*, respectively.

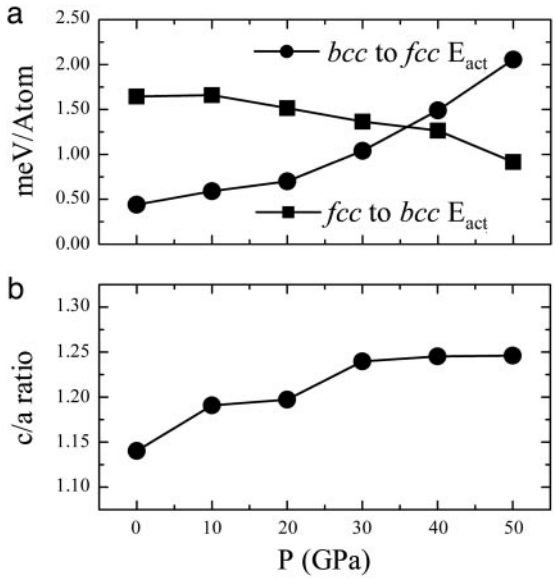

Fig. 4. Pressure dependence of two key transformation quantities. (*a*) E_{act} for both the *bcc* to *fcc* and the *fcc* to *bcc* transformations. (*b*) *c*/*a* ratio at the transition state.

transformation region, only a very small energy per atom could allow such transformations to occur.

Fig. 4*b* displays the c/a ratio at the TS as a function of pressure. The TS has $c/a = 1.14$ at zero pressure, but the TS c/a ratio increases rapidly with pressure until it plateaus at $c/a \approx 1.25$. Just as in molecular systems obeying the Hammond postulate (26), such a shift in TS structure is not unexpected, because transition states are often shifted toward the high energy end of the MEP.

Fig. 3*b* shows the magnitude of the true stress tensor ($|\boldsymbol{\sigma}_t|$) along the MEP. We see that the SSNEB algorithm predicts zero stress in the transition state, as it should. Note that the stress at the TS is not exactly zero for some pressures. This is not an artifact of the algorithm; it is just that these small stresses approach the accuracy limit of current OF DFT simulations. The more close-packed, *fcc*-to-TS portion of the MEP appears to plateau in stress as the pressure is increased. However, the more open-structured, *bcc*-to-TS portion of the MEP varies significantly with pressure, with the MEP under increasing stress with increasing pressure. This increase in $|\boldsymbol{\sigma}_t|$ over the *bcc* to TS portion of the MEP is consistent with the increase in E_{act} over the same portion of the MEP. These findings are not surprising, since the path from *bcc* to *fcc* involves expansion, and therefore increasing pressure works against this path, leading to higher energies and higher stresses.

Fig. 3*c* shows the pressure dependence of the volume per atom along the MEP with respect to the volume per atom of the relaxed *bcc* phase. We observe that the transition state appears as a local maximum in volume at all applied pressures, suggesting that maximum distortion is required at the saddle point in strain space. Pressure significantly influences the magnitude of the volume fluctuations along the MEP, for example by decreasing the local volume maxima at the TS. At high enough pressures, we see that this volume maximum at the TS is nearly completely suppressed.

Predictions for properties of the *bcc* to *hcp* transformation at zero pressure are shown in Fig. 5. In particular, Fig. 5*a* shows the energy per atom during the transformation, where we see that the energy varies smoothly, with an extremely small E_{act} quite similar to the *bcc* to *fcc* transformation. Fig. 5*b* shows the $\boldsymbol{\sigma}_t$ and internal pressure (one-third the trace of $\boldsymbol{\sigma}_t$) as a function of Δ, where Δ has the same meaning as above except the maximum Δ now represents the completely relaxed *hcp* phase. We see again that the algorithm predicts $\boldsymbol{\sigma}_t = 0$ (and consequently $P = 0$) at the TS, as it should. Fig. 5*c* displays the volume per atom during the transformation. Interestingly, here the TS is not a local maximum as it was during the *bcc* to *fcc* transformation. This may be due to the more complex pathway involved, where unlike the *bcc* to *fcc* transformation, there is a shuffle of nuclei during the *bcc* to *hcp* transformation.

To investigate the validity of the RNM approximation, we examine how the atomic positions vary during the transformation; this corresponds to the shuffle, **u**, which is represented in Fig. 5*d* by the variation in the second fractional coordinate of atom two ($\mathbf{r}^{II}[2]$), in the *bcc* reference frame. The transformation proceeds from *bcc* to *hcp* in three stages. Initially, the transformation is simply a deformation of the bulk *bcc* phase, indicated by the value of $\mathbf{r}^{II}[2]$ being nearly zero for the first three images. Then, nuclear motion begins near the third image, as shown by the "first-order-like" behavior of $\mathbf{r}^{II}[2]$; i.e., the first derivative of $\mathbf{r}^{II}[2]$ appears to be discontinuous with respect to the transformation path. Finally, the transformation is completed by $\mathbf{r}^{II}[2]$ smoothly approaching the *hcp* value. The continuous motion of $\mathbf{r}^{II}[2]$ as a function of Δ helps validate the RNM approximation, since discontinuous atomic motion would be unphysical and would invalidate the approximation.

Conclusions

We have developed a method by which transition states can be found for solid–solid phase transitions. The method is based on the CINEB scheme, where we recast the key quantities from a force–position formalism into a stress–strain formalism. We employ a RNM approximation, where we assume that atomic motion is much faster than bulk crystal reshaping. This approximation allows us to decouple the atomic degrees of freedom from the six lattice degrees

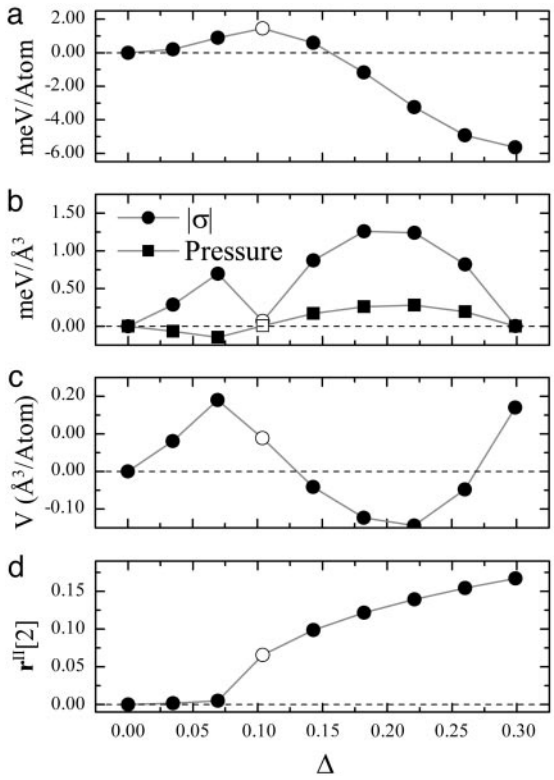

Fig. 5. Predicted properties of the *bcc* to *hcp* transformation in vacuum. (*a*) Energy per atom (*E*). (*b*) Magnitude of the true stress ($|\sigma|$) and the pressure (*P*). (*c*) Volume per atom (*V*). (*d*) Change in the fractional coordinate of the shuffled atom ($r^{II}[2]$). In all plots, the symbols represent points along the MEP, where the first and last represent the undeformed *bcc* and *hcp* phases, respectively, and where the open symbols represent the transition state.

of freedom. As a result, the transformation will be exclusively a function of the lattice degrees of freedom.

We then used the SSNEB method to explore elementary phase transformations in lithium metal. The method was shown to yield physically reasonable behavior for two different transformation paths, predicting the TS to have zero stress and zero force on the nuclei. The method predicts extremely small E_{act}s in all cases. These small energy barriers are to be expected for martensitic transformations, where the transformation mechanism is long-range and largely concerted. Therefore, to determine the actual activation energy for the transformation, the activation energies that we report here must be multiplied by the size of the transformation region, resulting in a significant energy barrier.

We find that pressure has an effect on these transformations by destabilizing the overall MEP with increasing pressure. Given that the transitions we examined (body-centered-cubic to close-packed phases) involve lattice expansions, this finding that increasing external pressure produces higher energies and stresses along the paths makes sense. We also observe that the molecular-based notion of the Hammond postulate appears to carry over to solid–solid phase transformations. Namely, the TS is generally shifted toward the high energy side of the MEP. Finally, the smooth nuclear motion demonstrated in the *bcc* to *hcp* transformation validates our RNM approximation.

The method does have limitations. Clearly, if the RNM approximation breaks down, this method is not valid. Also, nucleation-based phase transformations cannot be described by our algorithm. The model currently does not account for an imposed external field; however, this formalism should be easily extendable to a case where the stress tensor is no longer symmetric. Finally, the method finds the MEP as usual at zero Kelvin, forming the basis for understanding of the transformation at finite temperature, but says nothing about finite temperature effects.

Limitations not withstanding, this method is valid for materials undergoing martensitic transformations. In these cases, we can extract energy barriers, yielding not only the transformation properties but also information and insight into phase transformation mechanisms and kinetics. More specifically, by comparing the ratios for various activation energies, it may be possible to estimate the temperature hysteresis width, as well as the transformation front velocity, which also must depend on the transformation energetics. We envision use of this MEP at finite temperature to follow the dynamics of the phase transition, by using rare event methods (27–30).

This work was supported by the ASCI/ASAP Center for the Simulation and Dynamic Response of Materials at the California Institute of Technology and by the Air Force Office of Scientific Research.

1. Eyring, H. (1935) *J. Chem. Phys.* **3,** 107–115.
2. Born, M. & Oppenheimer, J. R. (1927) *Ann. Phys. (Leipzig)* **84,** 457–484.
3. Jónsson, H., Mills, G. & Jacobsen, K. W. (1998) in *Classical and Quantum Dynamics in Condensed Phase Simulations*, eds. Berne, B. J., Ciccotti, G. & Coker, D. F. (World Scientific, Teaneck, NJ), pp. 385–404 .
4. Ionova, I. V. & Carter, E. A. (1993) *J. Chem. Phys.* **98,** 6377–6386.
5. Ionova, I. V. & Carter, E. A. (1995) *J. Chem. Phys.* **103,** 5437–5441.
6. Elber, R. & Karplus, M. (1987) *Chem. Phys. Lett.* **139,** 375–380.
7. Gillilan, R. E. & Wilson, K. R. (1992) *J. Chem. Phys.* **97,** 1757–1772.
8. Henkelman, G., Uberuaga, B. P. & Jónsson, H. (2000) *J. Chem. Phys.* **113,** 9901–9904.
9. Henkelman, G. & Jónsson, H. (1999) *J. Chem. Phys.* **111,** 7010–7022.
10. Trinkle, D. R., Hennig, R. G., Srinivasan, S. G., Hatch, D. M., Jones, M. D., Stokes, H. T., Albers, R. C. & Wilkins, J. W. (2003) *Phys. Rev. Lett.* **91,** 025701.
11. Hennig, R. G., Trinkle, D. R., Bouchet, J., Srinivasan, S. G., Albers, R. C. & Wilkins, J. W. (2005) *Nat. Mater.* **4,** 129–133.
12. Andersen, H. C. (1980) *J. Chem. Phys.* **72,** 2384–2393.
13. Parrinello, M. & Rahman, A. (1980) *Phys. Rev. Lett.* **45,** 1196–1199.
14. Wentzcovitch, R. M. (1991) *Phys. Rev. B* **44,** 2358–2361.
15. Young, D. A. (1991) *Phase Diagrams of the Elements* (Univ. of California Press, Berkeley).
16. Crisp, R. S. (1991) *J. Phys. Condens. Matter* **3,** 5761–5768.
17. Burgers, W. G. (1934) *Physica* **1,** 561–586.
18. Watson, S. C. & Carter, E. A. (2000) *Comp. Phys. Comm.* **128,** 67–92.
19. Wang, Y. A., Govind, N. & Carter, E. A. (1999) *Phys. Rev. B* **60,** 16350–16358.
20. Watson, S., Jesson, B. J., Carter, E. A. & Madden, P. A. (1998) *Europhys. Lett.* **41,** 37–42.
21. Anta, J. A. & Madden, P. A. (1999) *J. Phys. Condens. Matter* **11,** 6099–6112.
22. Ceperley, D. M. & Alder, B. J. (1980) *Phys. Rev. Lett.* **45,** 566–569.
23. Perdew, J. P. & Zunger, A. (1981) *Phys. Rev. B* **23,** 5048–5079.
24. García, A., Elsässer, C, Zhu, J., Louie, S. G. & Cohen, M. L. (1992) *Phys. Rev. B* **46,** 9829–9832.
25. Juan, Y. M. & Kaxiras, E. (1993) *Phys. Rev. B* **48,** 14944–14952.
26. Hammond, G. S. (1955) *J. Am. Chem. Soc.* **77,** 334–338.
27. Bennett, C. H. (1997) in *Algorithms for Chemical Computations*, ACS Symposium Series, ed. Christofferson, R. E. (Am. Chem. Soc., Washington, DC), Vol. 46, pp. 63–97.
28. Chandler, D. (1978) *J. Chem. Phys.* **68,** 2959–2970.
29. Torrie, G. M. & Valleau, J. P. (1977) *J. Comp. Phys.* **23,** 187–199.
30. Carter, E. A., Ciccotti, G., Hynes, J. T. & Kapral, R. (1989) *Chem. Phys. Lett.* **156,** 472–477.